Current oscillations in solid oxide fuel cells underweakly humidified conditions

Sands, J. D.; Uddin, J.; Needham, D. J.

DOI:
10.1149/2.0701608jes

Document Version
Peer reviewed version

Citation for published version (Harvard):
Sands, JD, Uddin, J & Needham, DJ 2016, 'Current oscillations in solid oxide fuel cells underweakly humidified conditions', *Journal of the Electrochemical Society*, vol. 163, no. 8, pp. F856-F862. https://doi.org/10.1149/2.0701608jes

Current Oscillations in Solid Oxide Fuel Cells Under Weakly Humidified Conditions

J. D. Sands[a], J. Uddin[b], D. J. Needham[b]

[a]*School of Chemical Engineering, University of Birmingham, Edgbaston, Birmingham, B15 2TT, United Kingdom*
[b]*School of Mathematics, University of Birmingham, Edgbaston, Birmingham, B15 2TT, United Kingdom*

Abstract

In this paper we investigate the oscillatory response of a methane fuelled solid oxide fuel cell (SOFC) under weakly humidified conditions. Experiments have been conducted using operating conditions which allow for direct comparison with the mathematical model presented in [Sands et al. 2014]. There is good agreement between the experimental results and the predictions of the model, including transitions from a stable, steady current producing state, to nonlinear autonomous oscillations, to a zero current output state. The model from [Sands et al. 2014] is briefly summarised, followed by a description of the cell assembly and experimental procedures. The results are then presented followed by a discussion and comparison with the model.

Keywords:
solid oxide fuel cells, current oscillations, dynamical systems

1. Introduction

Oscillations of both voltage and electric current are well known phenomena within the solid oxide fuel cell (SOFC) community, and have been observed under fairly general conditions (see [2–11]). Many of the published results on SOFC oscillations consider specially designed cells or nonstandard operating conditions. For example, Wang et al. [7] recorded voltage oscillations in single chamber solid oxide fuel cells (SC-SOFC), which they attribute to cyclic oxidation/reduction cycles of the anode material due to the inclusion of oxygen in the fuel stream. Voltage oscillations were also observed in standard SOFCs by Marina et al. [3] when selenium was added to the

fuel stream in order to simulate a contaminated fuel supply. They believe that periodic adsorption/desorption of selenium on the anode surface caused variance in the cell polarisation which led to the observed voltage oscillations. Additionally, Huang et al. [10] conducted experiments on an SOFC with an anode made from a composite of lanthanum strontium cobaltite ferrite and gadolinium doped ceria (LSCF-GDC) and found current oscillations when using methane as the primary fuel. This particular anode composition catalytically favours direct oxidation of methane, as well as methane dissociation. The driving factor behind these oscillations was believed to have been the build of oxygen vacancies in the bulk of the anode due to the oxidation of carbon species which are produced from methane dissociation on the LSCF-GDC catalyst, which eventually lead to cyclic oxidation/reduction cycles of the anode material. The cell configurations and operating conditions found in the literature surrounding SOFC oscillations differ from the standard setup as given in [12]. Generally SOFCs use a dual chamber configuration with a composite formed of nickel and yttria-stabilised zirconia (Ni/YSZ) as the anode material. This anode composition catalytically favours the steam reforming reactions [13]. A variety of hydrocarbons can be used, but methane has become popular due to it's availability. In order to maximise the life time of the cell, the fuel is normally cleaned to remove impurities, and sealed so that oxygen does not reach the anode. Water, in varying amounts, is commonly added to the fuel stream in the gas phase, both to promote hydrocarbon steam reforming, as well as to prevent carbon deposition.

Until recently there had been no publications on oscillations in the standard methane fuelled SOFC as described above. However, a theoretical investigation was conducted in order to elucidate the oscillatory mechanism for the standard cell configuration, through a first principles mathematical model, based on fundamental chemical kinetics and Fickian mass transfer [1]. A coupled system of nonlinear ordinary differential equations was derived which captured the chemical and mass transfer effects which take place at the anode of a dual chamber, methane fuelled SOFC, utilising a porous Ni/YSZ anode, and assuming no extraneous species other than the desired fuel. The system was nondimensionalised and then rationally reduced to a planar dynamical system based on typical operating conditions. The analysis of this planar dynamical system was then split into two cases, namely, a weakly humidified, and a fully humidified fuel stream. The case of a weakly humidified fuel stream was examined in detail in [1]. The model exhibited multiple steady states and autonomous nonlinear oscillations in the phase

plane. Regions of parameter space were identified and sketched in the unfolding plane, describing the qualitatively different behaviours of the system.

One of the interesting features of the model is that there exists a zero current output state for a low enough, but still greater than zero, concentration of methane. For a fixed low (or zero) concentration of water (as steam) in the fuel stream, this corresponds with a nonreactive state, where the concentration of methane fed into the fuel cell effectively stays the same, and no current is produced. The region of oscillations is predicted to occur just before the zero current output state, as the concentration of methane is decreased during standard SOFC operation.

A series of experiments have been conducted in order to investigate the oscillatory phenomena occurring in standard methane fuelled SOFCs with a Ni/YSZ anode. In this paper the results of this experimental programme are presented, and we compare them with the results of the model presented in [1]. To begin with, the model is briefly summarised and the notation is introduced. The parameters which are used as inputs to the model are then presented, followed by a description of the experimental setup. The results are presented in Section (4.4) and then compared with the model in Section (5). Good agreement is found between the experimental and theoretical results.

2. Model Overview

The principal electrochemical and chemical reactions which take place within the Ni/YSZ anode of an SOFC operated on methane, using the internal reforming method, are given by Singhal & Kendall [12] as,

$$CH_4 + H_2O \rightarrow CO + 3H_2 \quad : \quad k_1[CH_4][H_20] \qquad (1)$$

$$CO + H_2O \rightarrow CO_2 + H_2 \quad : \quad k_2[CO][H_20] \qquad (2)$$

$$2H_2 + O_2 \rightarrow 2H_2O \quad : \quad k_3[H_2]^2[O_2] \qquad (3)$$

$$2CO + O_2 \rightarrow 2CO_2 \quad : \quad k_4[CO]^2[O_2] \qquad (4)$$

Here k_i, $(i = 1, 2, 3, 4)$, are the reaction rate constants for each respective reaction step. The reactions (1)-(4) will be adopted as the fundamental reaction scheme where (1) is the endothermic steam reforming of methane, (2) is the slightly exothermic water-gas shift (WGS) reaction, (3) and (4) are the electrochemical oxidation of hydrogen and carbon monoxide respectively.

In the electrochemical reactions (3) and (4) electrons are liberated, then the current is collected and distributed along an external circuit.

A simplification can be made to the reaction scheme (1)-(4), since the reaction given by (2) proceeds much faster than the other reactions [14–17]. In general, for reactions (1)-(4) in SOFCs it has been confirmed (see for example [12, 14, 15]), that,

$$k_2 \gg \frac{k_1[CH_4]}{[CO]}, \tag{5}$$

$$k_2 \gg \frac{k_3[H_2]^2[O_2]}{[CO][H_2O]}, \tag{6}$$

$$k_2 \gg \frac{k_4[CO][O_2]}{[H_2O]}, \tag{7}$$

which allows us to reduce the reaction scheme (1)-(4) to,

$$CH_4 + 2H_2O \rightarrow CO_2 + 4H_2 \quad : \quad k_1[CH_4][H_20] \tag{8}$$

$$2H_2 + O_2 \rightarrow 2H_2O \quad : \quad k_3[H_2]^2[O_2] \tag{9}$$

with the composite reaction (8) being governed by the slowest component rate of reaction. This reduction is supported by Ho et al. [16] who note that the reaction step (2) reaches equilibrium because it is kinetically fast and almost all of the CO is consumed in this reaction. Any remaining CO may participate in the reaction given by (4) which contributes electrical current, however the CO oxidation rate is around $2-3$ times slower than that of hydrogen oxidation. Hence the dominant current contribution is from hydrogen oxidation alone. This is confirmed by Yakabe et al. [17] who found that the WGS reaction (2) was fast enough to significantly reduce the concentration polarization downstream of the fuel inlet.

It is worth observing at this stage, that if we (tentatively) regard reaction (8) as significantly faster than reaction (9), then these two reactions may be combined to give, overall,

$$CH_4 + O_2 + 2H_2 \rightarrow CO_2 + 4H_2 \quad : \quad k_3[H_2]^2[O_2] \tag{10}$$

which is a cubic autocatalytic reaction, with reactant CH_4, pool chemical O_2, and autocatalyst H_2. The effect of Fickian transfer in CH_4 and H_2O, with O_2 acting as a pool chemical, puts this cubic autocatalytic reaction in

a continuous stirred-tank reactor (CSTR) environment. It is well established that cubic autocatalytic reactions in appropriate CSTR environments can sustain autonomous nonlinear oscillatory regimes (see, for example, Gray and Scott [18]). This gives us confidence that at the anode of an SOFC, it is the core chemistry encapsulated in reactions (8)-(9), when coupled with Fickian transfer from the fuel stream, which provides the principle mechanism of self-sustained autonomous oscillations observed in SOFCs.

The chemical concentrations of the reactant species are now introduced as,

$$[CH_4] = a, \tag{11}$$

$$[H_2] = b, \tag{12}$$

$$[H_2O] = c, \tag{13}$$

$$[O_2] = x. \tag{14}$$

The system of coupled nonlinear ordinary differential equations governing the reaction dynamics and transfer at the anode is given as (see [1]),

$$\dot{a} = \frac{D_a A}{V h}(a_0 - a) - k_1 a c, \tag{15}$$

$$\dot{b} = -\frac{D_b A}{V h} b + 4k_1 a c - 2k_3 b^2 x, \tag{16}$$

$$\dot{c} = \frac{D_c A}{V h}(c_0 - c) + 2k_3 b^2 x - 2k_1 a c, \tag{17}$$

where the dots above the variables represent differentiation with respect to time, t. The parameters D_a, D_b and D_c are respectively, the effective diffusion coefficients for the Fickian transfer of methane, hydrogen and water (as steam) to the reaction site, and h is the scale thickness of the anode. The coefficient $\frac{A}{V}$ is the surface area of transfer to volume ratio, whilst a_0 and c_0 represent the inlet concentrations of species a and c respectively. The oxygen is supposed to be in plentiful supply, as a pool chemical, at fixed concentration x. The first term of each rate equation represents the transfer of the particular species into the reaction zone A, whilst the remaining terms represent the production/consumption of the species as given by the reduced reaction scheme (8) and (9). The system (15)-(17) is then nondimensionalised and rationally reduced to the planar dynamical system (see [1]),

$$\dot{a} = \bar{D}_a(\bar{a}_0 - a) - \frac{2ab^2}{(2a+1)}, \tag{18}$$

$$\dot{b} = -\bar{D}_b b + \frac{8ab^2}{(2a+1)} - 2b^2, \tag{19}$$

which determines the temporal dynamics of the concentrations ($a(t)$, $b(t)$) in the case of a weakly humidified fuel stream. The dimensionless parameters which appear in (18) and (19) are given by,

$$\bar{D}_b = \frac{D_b k_1}{D_c x k_3}, \quad \bar{D}_a = \frac{D_a k_1}{D_c x k_3}, \quad \bar{a}_0 = \frac{a_0}{a_s}, \tag{20}$$

where the concentration scale a_s is given by,

$$a_s = \frac{D_a A}{V h k_1} \tag{21}$$

The parameter $\bar{D}_a$ measures the ratio of the diffusivity of methane to the diffusivity of water into the reaction zone A. Similarly the parameter $\bar{D}_b$ measures the ratio of the diffusivity of hydrogen to the diffusivity of water into the reaction zone A. The parameter $\bar{a}_0$ represents the ratio of inlet concentration to the scaled concentration of methane (a_s). The bifurcation analysis of the system (18)-(19), which will be referred to as [D-S], is given in [1]. Some figures from [1] will be reproduced in Section (5) in order to compare the model with the experimental results. In the next section the physical parameters, D_a, D_b, D_c, k_1, k_3, x, and a_0 used as inputs to the model are estimated.

3. Physical Parameters

We appeal to the literature, in order to obtain estimates of the physical parameters of the dynamcal system (18)-(19) as inputs to the model. Structural properties of the cell are required, and empirical data is taken for reaction rate constants and diffusion coefficients.

3.1. Diffusion Model

For multi-component diffusion in a porous membrane, the parallel pore model is used [17, 19] and effective diffusion coefficients for use with a Fickian

mass transport mechanism are obtained. For each species, i,

$$D_i^{eff} = \frac{\varphi}{\tau}\left(\frac{1-\alpha_{i,m}X_i}{D_{i,m}} + \frac{1}{D_i^{Kn}}\right)^{-1}, \tag{22}$$

where,

$$\alpha_{i,m} = 1 - \left(\frac{M_i}{M_{avg}}\right)^{-1}, \tag{23}$$

$$D_{i,m} = \frac{1-X_i}{\sum_{j\neq i}\frac{X_j}{D_{ij}}}. \tag{24}$$

Here, φ and τ are the anode porosity and tortuousity respectively, X_j is the mole fraction of species j, M_i is the molecular mass of species i, M_{avg} is the average molecular mass of the mixture, D_i^{Kn} is the Knudsen diffusion coefficient of species i, and D_{ij} is the binary diffusion coefficient of species i and j.

The average molecular mass of the mixture is given by the total mass of the mixture divided by the total moles of the mixture [20]. We can hence derive an expression for M_{avg} in terms of the mole fractions of the species and their respective molecular masses, as,

$$M_{avg} = \frac{m}{n} \tag{25}$$

$$= \frac{\sum n_i M_i}{n} \tag{26}$$

$$= \frac{\sum x_i n M_i}{n} \tag{27}$$

$$= \sum x_i M_i \tag{28}$$

where x_i is the mole fraction of species i, n_i is the number of moles of species i, m is the total mass of the mixture, and n is the total moles of the mixture.

The Knudsen diffusion coefficient is given by [17],

$$D_i^{Kn} = \frac{2}{3} r_p \left(\frac{8R_u T}{\pi M_i}\right)^{\frac{1}{2}}, \tag{29}$$

where, r_p is the average pore radius of the anode, R_u is the universal gas constant, and T is the temperature in Kelvin.

The binary diffusion coefficients used in equation (22) come from the first order approximation to the Chapman-Enskog theory for binary mixtures [21], that is,

$$D_{ij} = 0.0018583 \quad T^3 \quad \frac{1}{M_i} + \frac{1}{M_j} \quad \frac{1}{p\sigma_{ij}^2 \Omega_{ij}}, \tag{30}$$

where, p is pressure of the gas mixture and σ_{ij} is the average collision diameter given by,

$$\sigma_{ij} = \frac{\sigma_i + \sigma_j}{2}. \tag{31}$$

The path integral, Ω_{ij}, is empirically derived as,

$$\Omega_{ij} = \frac{1.06036}{(T^*)^{0.15610}} + \frac{0.19300}{e^{0.47635T^*}} + \frac{1.03587}{e^{1.52996T^*}} + \frac{1.76474}{e^{3.89411T^*}} \tag{32}$$

where,

$$T^* = \frac{k_B T}{_{ij}}, \tag{33}$$

and the characteristic energy is,

$$_{ij} = \sqrt{}_{i\ j}. \tag{34}$$

Here, k_B is the Boltzmann constant, whilst σ_i, σ_j, $_i$, and $_j$ are Lennard-Jones parameters which are given by Mason & Monchick [22] and Roncin [23], for the species under consideration. For comparison with the model we take $D_a = D_a^{eff}$, $D_b = D_b^{eff}$, and $D_c = D_c^{eff}$.

3.2. Reaction Kinetic Model

Many studies have been done on the rate of methane steam reforming in SOFCs [24–27] which indicate that the rate of steam reforming is much higher than the rate of hydrogen oxidation. An expression for the rate constant for

the steam reforming of methane has been given as [25, 28],

$$k_1 = S_A^{Ni} 0.0636 T^2 e^{\frac{-27063}{T}}, \tag{35}$$

where, S_A^{Ni} is the specific surface area of the nickel catalyst in the SOFC anode ($\frac{m^2}{m^3}$). Values of S_A^{Ni} generally used in the literature for SOFC modelling are estimated to be between 2×10^5 and 1×10^6, however a comprehensive study of anode structural properties under redox cycling has more recently been done, estimating the specific surface area of nickel to be between 3.56×10^6 and 5.86×10^6 [29]. The study determined the anode structural properties before and after a number of redox cycles using Focussed Ion Beam Scanning Electron Microscopy. The results, in fact, showed that S_A^{Ni} increased monotonically as the number of redox cycles increased.

The reaction rate constant for hydrogen oxidation, k_3, may be estimated via an application of Faraday's law of electrolysis.

$$\frac{i}{VnF} = 2k_3 b^2 x, \tag{36}$$

where, i is the current drawn from the cell (A), V is the volume of the anode (m^3), n is the change in valence of the reactant, F is Faraday's constant ($\frac{C}{mol}$), b and x are the concentrations of hydrogen and oxygen respectively ($\frac{mol}{m^3}$), and so,

$$k_3 = \frac{i}{2VnFb^2x} \tag{37}$$

3.3. Stoichiometry

Since the cell will be exposed to air at 1073 K, the value of x, which is the concentration of oxygen at the cathode side ($\frac{mol}{m^3}$), is calculated as follows. Assuming air contains approximately 21% oxygen by volume, and taking 100 m^3 of air as a basis, we have,

$$x = \frac{\text{mass of } O_2}{\text{molar mass of } O_2} \frac{1}{\text{volume of air}} \tag{38}$$

$$= \frac{\text{density of } O_2 \text{ at } 1073K \times \text{volume of } O_2}{\text{molar mass of } O_2} \frac{1}{\text{volume of air}} \tag{39}$$

$$= \frac{0.3633 \frac{kg}{m^3} \times 21 m^3 \quad 1}{0.032 \frac{kg}{mol} \qquad 100 m^3} \tag{40}$$

$$= 2.3842 \frac{mol}{m^3}. \tag{41}$$

The concentration of methane in the fuel channel, a_0, is calculated as,

$$a_0 = \frac{\text{molar flow rate of } CH_4 \frac{mol}{s}}{\text{total flow rate} \frac{m^3}{s}} \tag{42}$$

$$= \frac{\text{mass flow rate of } CH_4 \frac{kg}{s}}{\text{total flow rate} \frac{m^3}{s} \times \text{molar mass of } CH_4 \frac{kg}{mol}} \tag{43}$$

$$= \frac{\text{density of } CH_4 \frac{kg}{m^3} \times \text{flow rate of } CH_4 \frac{m^3}{s}}{\text{total flow rate} \frac{m^3}{s} \times \text{molar mass of } CH_4 \frac{kg}{mol}}. \tag{44}$$

At high temperatures the ideal gas law may be applied [30], giving,

$$\rho_{CH_4} = \frac{P \times \text{molar mass of } CH_4}{RT}, \tag{45}$$

where ρ_{CH_4} is the density of methane, P is the pressure, R is the universal gas constant and T is the temperature. Substituting into equation (44) we arrive at,

$$a_0 = \frac{\dot{Q}_{CH_4} \quad P}{\dot{Q}_{Tot} \quad RT} \tag{46}$$

$$= \frac{\dot{Q}_{CH_4} \qquad 101325 Pa}{\dot{Q}_{Tot} \quad 8.314 \frac{m^3 \, Pa}{mol K} \times 1073 K} \tag{47}$$

$$= 11.3581 \times \frac{\dot{Q}_{CH_4} \, mol}{\dot{Q}_{Tot} \quad m^3}. \tag{48}$$

Here, $\dot{Q}_{CH_4}$ is the volumetric flow rate of methane ($\frac{m^3}{s}$), and $\dot{Q}_{Tot}$ is the total fuel stream flow rate ($\frac{m^3}{s}$). The surface area of transfer, A, and the thickness of the anode, h, are used to calculate the dimensionless parameters that were introduced in [1].

4. Experimental

A preliminary test was first performed on a microtubular SOFC as was used in [31], whilst subsequent experiments were conducted using tubular SOFCs, assembled in-house, with the geometry as shown in Figure (1).

The experiments performed here were done with low fuel stream humidification ($\leq$ 2%), corresponding with the dynamical system [D-S] as given in equations (18)-(19). According to the model, introducing higher concentrations of steam creates more variable behaviour, and would require a more comprehensive study than the present experimental programme. The aim of this experimental programme is to establish preliminary results, and test fundamental model predictions for the case of a weakly humidified fuel stream. Thus we start with the experimental conditions which correspond with $\bar{c}_0 \ll 1$.

4.1. Cell Assembly

The anode supported microtubular cell came from the same batch of cells that were prepared in [31], and the dimensions were approximately 55mm in length, with an inside diameter of 2.2mm, and outside diameter of 2.8mm. The approximate thicknesses of each layer were, 300μm of Ni anode, 15μm of YSZ electrolyte, and 30μm of LSM cathode. In order to collect the current, a 10mm strip of the YSZ electrolyte was carefully filed down in order to expose the Ni anode beneath. Conducting silver ink was then applied to both electrodes. The exposed anode was completely covered by the ink, whilst the cathode only had 4 bands of silver ink in order to minimise oxygen concentration polarisation. Silver wire was then tightly wrapped around the cell electrodes, in contact with the applied silver ink. The cell manifolds were made from drilled macor blocks, and the cell was held in place using high temperature cement, with silver ink applied over the top in order to minimise leakage. The outlet manifold was connected to an exhaust pipe and once again sealed with high temperature cement and silver ink. This was to ensure that there was no combustion near the outlet due to leaked fuel, which has been known to damage the cell [32].

The anode supported tubular cells were commercially obtained with the configuration as shown in Figure (1). A similar method to the preparation of the microtubular cells was used, with a 10mm strip of anode being exposed by filing down the samarium doped ceria (SDC) barrier and YSZ electrolyte. Silver ink was then applied to the entire exposed anode, and in 4 bands

along the cathode. The cell was sintered at 120^oC for 2 hours before tightly wrapping the silver wire around the cell electrodes. More silver ink was then applied on top of the silver wire, carefully filling in the gaps between the wire and the silver-coated electrodes. The cell was again sintered at 120^oC for a further 2 hours in order to enhance the electrical contact. The cell manifolds were made from drilled macor cylinders, and the connecting tubes were made from alumina. At the inlet the alumina tube was connected to the piping coming from the fuel supply, whilst the outlet alumina tube was connected to an exhaust pipe. All the connections were sealed with high temperature cement, and the connections between the cell and the manifolds also had silver ink applied over the top in order to minimise leakage. The cell and manifolds are shown in Figure (2).

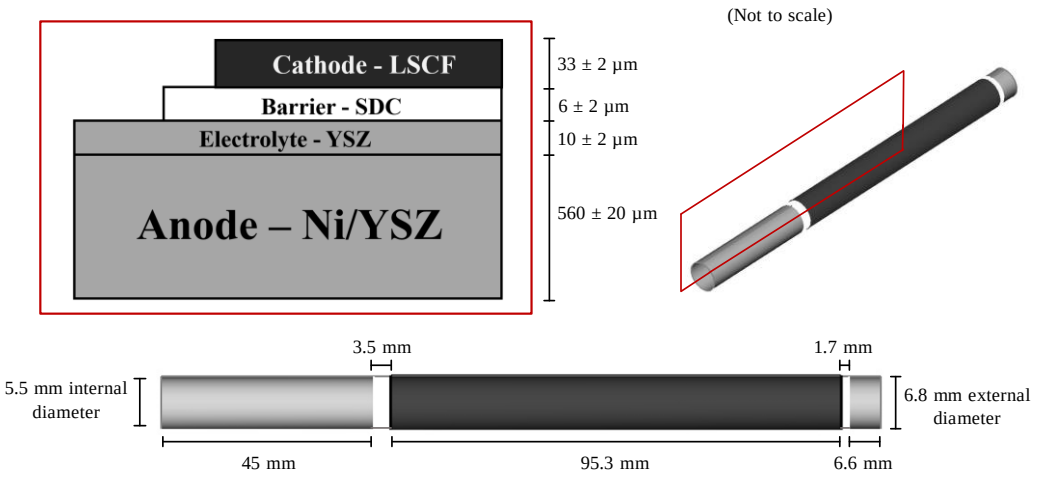

Figure 1: Tubular SOFC configuration.

4.2. Test Rig

Gas cylinders were connected to specific mass flow controllers, which in turn were fed into a gas mixer prior to entering the cell. The setup was such that the gas mixture could then either pass through a humidifier, or go directly into the cell. The piping from the gas mixer/humidifier was connected to the cell manifolds, whilst the outlet manifolds were connected to

Figure 2: Tubular SOFC with manifolds.

an exhaust pipe as described in section (4.1). The cell was enclosed in a high temperature, programmable furnace, and the silver wire current collectors were connected to a potentiostat. A schematic is shown in Figure (3).

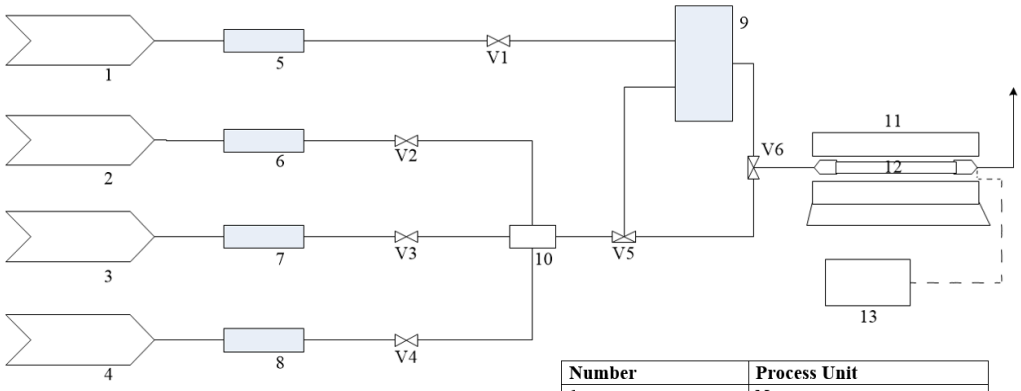

Number	Process Unit
1	N_2
2	H_2
3	CH_4
4	N_2
5-8	mass flow controller
9	evaporator/humidifier
10	gas mixer
11	furnace
12	tubular SOFC
13	potentiostat
V1-V4	quarter turn valve
V5, V6	three-way valve

Figure 3: Test rig schematic.

4.3. Experimental Procedure

We now detail the experimental procedure for the fuel cell assemblies described in the previous sections.

4.3.1. Microtubular SOFC

The microtubular cell was heated up to 700^oC, whilst maintaining a flow of H_2 through the cell at $30\frac{ml}{min}$. This was done in order to prevent the Ni anode from reoxidising. The open circuit voltage (OCV) was then measured for 40 minutes to allow the cell to stabilise. After the OCV test, the fuel stream was switched to a mixture of CH_4 and He, with a flow rate totalling $30\frac{ml}{min}$. The flow was allowed to stabilise, then a potentiostatic test was performed. The potential difference between the 2 cell electrodes was held at 0.5V throughout. This potential difference will henceforth be referred to as the applied voltage, or the voltage applied to the cell. The lower the applied voltage in these experiments, the faster we drive the forward hydrogen oxidation reaction (9). In the model this corresponds with an increasing k_3 (and hence via (20), a decrease in $\bar{D}_a$ and $\bar{D}_b$, with $\bar{a}_0$ remaining fixed), which in turn dictates the region of the unfolding plane in which the system is located, along with the other operating conditions and structural properties of the cell. Initially the concentration of CH_4 was kept low, and over regular time intervals the CH_4 flow rate would be increased by $0.5\frac{ml}{min}$, whilst the He flow rate would simultaneously be reduced by $0.5\frac{ml}{min}$ in order to maintain a reasonably constant flow rate. In this experiment there was no fuel stream humidification.

4.3.2. Tubular SOFC

The tubular cells were heated up to 800^oC, while once again, maintaining a flow of H_2 through the cell at $70\frac{ml}{min}$ to prevent the Ni anode from reoxidising. The OCV was then measured for 40 minutes to allow the cell to stabilise. After the OCV test, the fuel stream was switched to a mixture of CH_4, N_2, and H_2O, with a flow rate totalling approximately $100\frac{ml}{min}$. The flow was allowed to stabilise, then a potentiostatic test was performed. Initially the cell was held at an applied voltage of 0.8V. In this experiment the CH_4 flow rate was initially high, and was decreased after the dynamic behaviour of the cell became apparent. The N_2 flow rate was simultaneously increased by the same amount in order to keep the flow rate approximately the same. The minimum time between flow rate adjustment was set at 20 minutes, in order

to ensure the cell had reached a distinct stable, or oscillatory state. The potentiostatic experiment was then repeated for applied voltages of 0.7V and 0.6V, using the same procedure for adjusting the flow rates. Three different tubular cells were tested using this method.

4.4. Results

4.4.1. Microtubular SOFC

In what follows, all fuel compositions will be given in $\frac{ml}{min}$. The initial experiment with the microtubular cell utilised very dilute concentrations of dry methane. In Figure (4) an oscillatory response was observed after an initial settling in period of around 3 minutes. The concentration of methane was increased gradually over time starting at 5/25/0 (CH_4/He/H_2O), and the oscillations persisted up until the fuel composition reached 11.5/18.5/0 (CH_4/He/H_2O). At this concentration of methane, the cell was seen to undergo a qualitative change in behaviour. The amplitude of the oscillations decreased, as the average current increased, until a new quasi-steady state was reached at approximately 9380*s*.

4.4.2. Tubular SOFCs

For the first cell tested, steady states were observed for intermediate to high concentrations of methane in all potentiostatic experiments. For a fixed composition, the amount of current drawn from the cell increased as the applied voltage decreased, due to the accelerated forward electrochemical reaction (3). Additionally, as the concentration of methane in the fuel stream was decreased, the average current output also decreased due to a reduced flux of reactants into the anode. For applied voltages of 0.8*V* and 0.7*V*, the cell began to exhibit small fluctuations in current output at the lower concentrations of methane, and then dropped to a zero current state at compositions 5/93/2 and 5.5/92.5/2 (CH_4/N_2/H_2O) respectively. When the applied voltage was decreased to 0.6*V*, the cell exhibited self-sustained, autonomous current oscillations at low concentrations of methane. The initial step decrease in methane concentration was $2\frac{ml}{min}$, up until the region of oscillation. After 20 minutes, the concentration of methane was then increased by $0.5\frac{ml}{min}$, which caused the oscillations to decrease in amplitude, whilst the average current increased. After another 40 minutes the methane concentration was again increased by $0.5\frac{ml}{min}$, causing the oscillation amplitude to further decrease, and the average current to increase again. This effect is similar to that observed for the microtubular cell, where the initial state was

oscillatory, and increasing the methane concentration through a critical value caused a new quasi-steady state to be reached. Following this, the methane concentration was decreased sufficiently to bring the cell back into the fully oscillatory state, and then further decreased over time in order to observe the effect on the oscillations. At a composition of 5/100/2 ($CH_4/N_2/H_2O$) the cell dropped to a zero current state.

The second and third cells gave very similar performance to each other in terms of electrical output. The cells exhibited the same steady state behaviour as the first cell at intermediate and high concentrations of methane, for all applied voltages. However in these experiments, the step decrease in methane concentration was much smaller at lower concentrations. This was done in order to induce the oscillatory state before the zero current state was reached. Self-sustained, autonomous current oscillations were observed at all applied voltages in both cells. As the methane concentration was lowered, the oscillations generally increased in amplitude, whilst the average current decreased. In all cases the zero current state was reached for a non-zero concentration of methane in the fuel stream, however the critical values at which the zero current states occurred were lower for the second and third cells than that of the first cell. Additionally, when comparing the performance between the cells at the same fuel composition, the second and third cells provided much more current than the first cell, indicating a much more efficient SOFC. This explains, why at each of the applied voltages, the zero current state was reached at a lower methane concentration for the second and third cells. The difference in performance was no doubt an artefact of the cell assembly process. Interestingly, the peak of the current oscillations was still relatively high for methane-deprived compositions. For example, in the case of the second cell, at an applied voltage of $0.6V$ the current peaked as high as $0.7A$ for compositions as low as 0.5/100/2 ($CH_4/N_2/H_2O$). Regarding high power output in oscillatory modes of operation, in [33], a PEMFC was observed to oscillate under galvanostatic, but not potentiostatic conditions. The authors point out that for the same fuel compositions, the time-averaged power output density was much higher in the oscillatory state than in the corresponding steady state. This implies that it may be beneficial to operate the cell in oscillatory mode for any application whose power requirements are not strictly time dependent. For example, electrolysis is often used to produce hydrogen for fuel by passing an electric current through water. Since the hydrogen product is generally stored in gas cylinders for later use, it is not strictly necessary to produce the hydrogen at a constant rate. Thus, a

more efficient system is possible by supplying the current from an oscillatory mode of operation, as opposed to that from a steady state current output. Results from the potentiostatic experiment performed on tubular SOFC 2 at an applied voltage of $0.7V$ are presented in Figure (5).

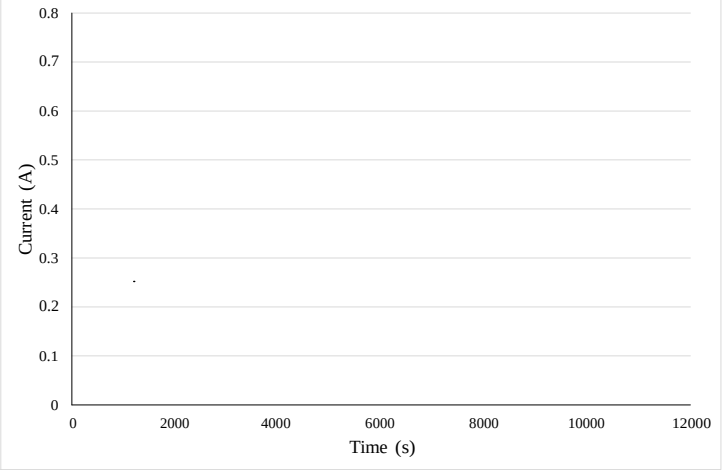

Figure 4: Potentiostatic experiment for microtubular cell at 0.5V. Here, the initial concentration of methane, a_0, is increasing with time.

5. Discussion

In this section we relate the experimental results from Section 4 to the model predictions from [1]. The first interesting feature is that the current drops to zero for a non-zero concentration of methane in the fuel stream. In other words, the fuel cell stops producing electric current when the amount of methane in the fuel channel drops below a critical value. This observation is in full accord with the predictions of the model, and the critical value is represented in the model by $\bar{a}_0^{SN}$, $\bar{a}_0^{P}$, or $\bar{a}_0^{\infty}$, which correspond with saddle-node, periodic saddle-node, and homoclinic bifurcations respectively, depending on which region of parameter space the fuel cell system corresponds with (see [1]). The model presented in [1] predicts a non-zero, current producing steady state or oscillatory response for $\bar{a}_0 > \bar{a}_0^{SN}$, $\bar{a}_0^{P}$, or $\bar{a}_0^{\infty}$, and a zero current output state for values of $\bar{a}_0 < \bar{a}_0^{SN}$, $\bar{a}_0^{P}$, or $\bar{a}_0^{\infty}$. For $\bar{D}_a \geq \bar{D}_a^*(\bar{D}_b)$, where $\bar{D}_a^*(\bar{D}_b)$

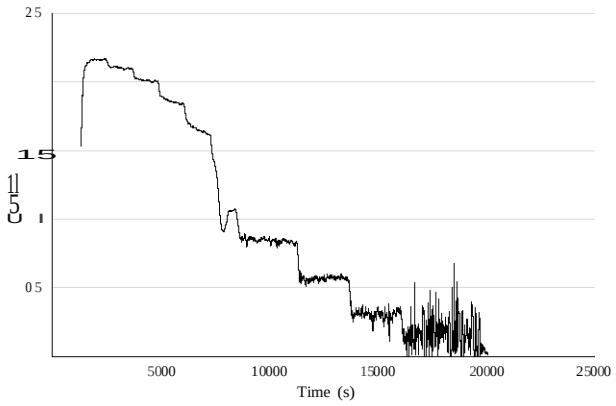

Figure 5: Potentiostatic experiment for tubular cell 2 at 0.7V. Here, the initial concentration of methane, ao, is decreasing with time.

is the value of *Da* below which there exist Hopf bifurcations, and above which no Hopf bifurcations exist, there are no limit cycles in the phase plane, and therefore one would not expect to observe an oscillatory response from the cell as appears to be the case in the first cell for applied voltages greater than 0.6V. However we shall see that the region of parameter space dictated by the experimental setup corresponds with points in the unfolding plane which give an oscillatory response over a certain range of a_0. The fact that no oscillations are observed in this case for the higher applied voltages is attributed to the step change in methane concentration being too large. The later experiments which use much smaller step changes in methane concentration show oscillations at all applied voltages. From [1] we define the equilibrium points e_ and e+ to be the equilibrium points arising from the saddle-node bifurcation agN, and the equilibrium point e_0 to be the equilibrium point corresponding with a nonreactive state. Decreasing the methane concentration below agN causes the equilibrium points e_ and e+ to collide via a saddle-node bifurcation, leaving only the equilibrium point e_0, which corresponds with a zero current output state. Thus we would expect to see the cell go from a non-zero stable current states, since the equilibrium point e_ corresponds with a stable steady state current output, to the zero current state, without exhibiting any oscillations. For all $0 < Da < D(Db)$, where $D(Db)$

corresponds with the critical value of $\bar{D}_a$ below which periodic saddle-node, Hopf, and homoclinic bifurcations may occur, stable limit cycles arise in the phase plane, so one would expect to see the cell exhibit autonomous current oscillations. For $\bar{D}_a^{\infty}(\bar{D}_b) < \bar{D}_a < \bar{D}_a^{c}(\bar{D}_b)$, where $\bar{D}_a^{\infty}(\bar{D}_b)$ corresponds with the value of $\bar{D}_a$ below which only homoclinic and Hopf bifurcations may occur, decreasing the methane concentration below $\bar{a}_0^P$ causes the stable and unstable limit cycles to collide via a periodic saddle-node bifurcation, leaving the equilibrium point $\mathbf{e_0}$ as the only stable attractor in the phase plane. Thus one would expect to see the cell go from a stable steady state, to an oscillatory state, and then finally to the zero current state. For $0 < \bar{D}_a \leq \bar{D}_a^{\infty}(\bar{D}_b)$, the mechanism would involve the stable limit cycle colliding with the equilibrium point $\mathbf{e}_+$ via a homoclinic bifurcation, leaving the equilibrium point $\mathbf{e_0}$ as the only stable attractor in the phase plane. Similarly, one would once again expect to see the cell go from a stable steady state, to an oscillatory state, and then to the zero current state, as the concentration of methane was lowered. All of these sequences of behaviour are seen in the experiments.

When we now look at the non-dimensional parameters in the model, we can determine the region of parameter space corresponding with the physical fuel cell setup, in the experiments, based on the operating conditions and material properties of the fuel cell. We have,

$$\bar{D}_b = \frac{D_b}{D_c} \frac{k_1}{xk_3}, \quad \bar{D}_a = \frac{D_a}{D_c} \frac{k_1}{xk_3}, \quad \bar{a}_0 = \frac{a_0}{a_s}.$$

From these we obtain the relationship,

$$\bar{D}_a = \frac{D_a}{D_b} \bar{D}_b. \tag{49}$$

The parameters D_a and D_b are the dimensional Fickian transfer coefficients, for methane and hydrogen respectively, which can be calculated from equation (22). For the operating conditions, and fuel cell materials used in the experiment, we find that,

$$0.3138 < \frac{D_a}{D_b} < 0.3393. \tag{50}$$

A graphical user interface was created in MATLAB and used to calculate the values of D_a and D_b over the range of operating conditions. The range of $\frac{D_a}{D_b}$ was found by substituting in the upper and lower bounds given in the literature for material properties [26, 28, 34], in conjunction with the flow

rates and operating conditions used in the experiments.

From the model we also have the parameterisation,

$$\bar{a}^* = \alpha + \frac{\alpha(2\alpha+1)(2\alpha-1)}{(6\alpha+1)}\bar{a}_0, \quad \bar{D}_a^* = \frac{(2\alpha-1)^3}{32\alpha^2}\bar{D}_b, \quad \bar{D}_a = \frac{(2\alpha-1)^3}{4\alpha}\bar{D}_b^2, \quad \alpha > \frac{1}{2},$$

for the unfolding point $(\bar{a}_0^*, \bar{D}_a^*)$ in the $(\bar{a}_0, \bar{D}_a)$ unfolding plane. Here, α is the equilibrium point for a at the unfolding point $(\bar{a}_0^*, \bar{D}_a^*)$. Taking derivatives and applying the chain rule we find that,

$$\frac{d\bar{D}_a^*}{d\bar{D}_b} \to 1, \text{ as } \alpha \to \frac{1}{2}, \tag{51}$$

$$\frac{d\bar{D}_a^*}{d\bar{D}_b} \to 0.75, \text{ as } \alpha \to \infty. \tag{52}$$

This means that the value of $\bar{D}_a$ obtained from the actual diffusion coefficients in equation (49), for each $\bar{D}_b$, will always be less than $\bar{D}_a^*$, for the operating conditions of the fuel cell in this particular experimental programme. Additionally, it has been confirmed through numerical investigation that the curve $\bar{D}_a = \bar{D}_a^c(\bar{D}_b)$ lies between the curve $\bar{D}_a = \bar{D}_a^*(\bar{D}_b)$, and the curve given by equation (49). Therefore one would expect to see oscillations, given the right fuel composition, regardless of the applied voltage as has been confirmed in the experiments. The situation is shown in Figure (6).

The experiments on the second and third tubular cells indeed show current oscillations at all applied voltages for low methane concentrations. However, the first cell appeared to only exhibit minor current fluctuations before the zero current output state was reached. The absence of larger, distinct oscillations in cell 1 may be down to the step change in methane concentration being too great. The final step size before the cell dropped to zero current was $0.5\frac{ml}{min}$ for the first cell, at applied voltages of $0.8V$ and $0.7V$. However, it is possible that the cell may have started to oscillate if a smaller step size had been used. An indicator of how sensitive the system is to qualitative changes in behaviour can be seen in the potentiostatic test on the second cell at $0.6V$. At step decrease in methane of $0.1\frac{ml}{min}$ was enough to cause the cell to change from exhibiting autonomous current oscillations, where the peak was still approximately $0.5A$, to a zero current output. Therefore it is reasonable to suggest that oscillations may have occurred in the first cell, if the final step size had been smaller. This is further confirmed by finding

oscillations at all applied voltages in the later cells, where a much smaller

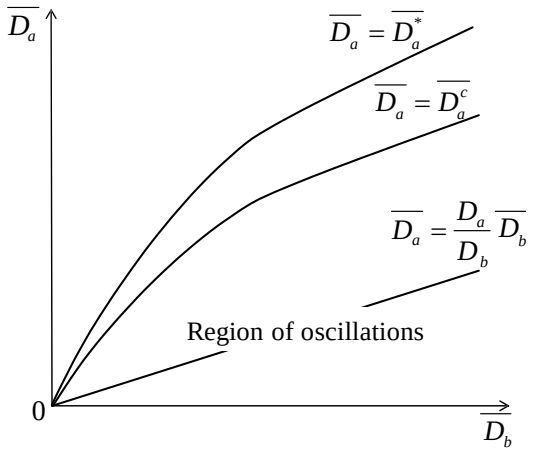

Figure 6: Sketch of $(\bar{D}_b, \bar{D}_a)$ plane.

step change in methane concentration was used.

We can infer other interesting features from the bifurcation diagrams shown in Figure 7. Figure 7a shows the full bifurcation diagram for fixed $0 < \bar{D}_a \leq \bar{D}_a^{\infty}$ in the $(\bar{a}_0, \alpha)$ plane, with the corresponding full bifurcation diagram in the $(\bar{a}_0, \beta)$ plane shown in Figure 7b. The amplitude of the oscillation is represented, in both Figure 7a and Figure 7b, by the line with an arrow in the centre, pointing in the direction of increasing amplitude. The equilibrium point $\mathbf{e}_- = (\alpha_-, \beta_-)$ corresponds with the stable, current generating state of the SOFC, whilst the equilibrium point $\mathbf{e_0} = (\bar{a}_0, 0)$ corresponds with the zero current output state. The value of β_- thus corresponds with the amount of current being produced in a steady state response from the cell, as given by equation (36). It can be seen from Figure 7b that as the initial concentration of methane is decreased (corresponding with a decrease in $\bar{a}_0$), the value of β_- also decreases, which, via (36), implies a decrease in current output. This trend can be seen in the experimental results for all 3 tubular cells. As can be seen in Figure 5, as the concentration of methane was decreased, the steady state current output decreased accordingly. To demonstrate this, we plot the steady state current output, against the concentration of methane supplied to the SOFC.

The results for the first cell, with an applied voltage of $0.7V$, are shown

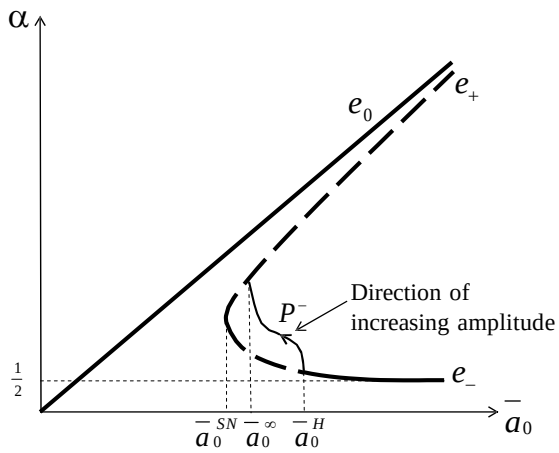

(a) ($\bar{a}_0$, α) plane.

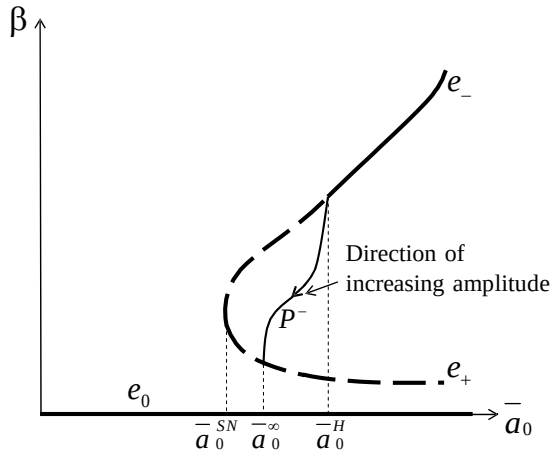

(b) ($\bar{a}_0$, β) plane.

Figure 7: Bifurcation diagrams in the (α, $\bar{a}_0$) and (β, $\bar{a}_0$) planes.

in Figure 8. The crosses are time averaged current outputs for various fuel compositions, and the dotted line is a cubic polynomial fit. The shape of the curve in Figure 8 matches very well with the $\mathbf{e}_-$ curve in Figure 7b,

validating the assumption that the concentration of hydrogen within the anode is representative of the current drawn from the cell at given operating conditions. With regard to the oscillations, it can be seen from Figure 7b

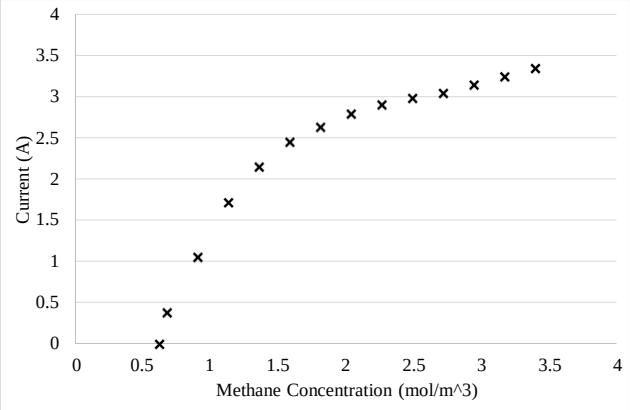

Figure 8: Steady state current output vs. methane concentration for cell 1 at an applied voltage of $0.7V$.

that first as the concentration of methane is decreased, the steady state current output decreases, then small amplitude oscillations arise in the phase plane surrounding the equilibrium point $\mathbf{e}_- = (\alpha_-, \beta_-)$. Further decreasing the concentration of methane lowers the value of β_-, whilst simultaneously increasing the amplitude of the oscillation. Physically this corresponds with less hydrogen in the anode, and therefore a lower average current output, with a larger amplitude of current oscillation. This trend can be be seen in Figure 5. As the cell is transitioning from steady state to oscillatory, the average current drops with each step decrease in methane concentration, whilst the amplitude of the oscillation increases. Conversely, with the microtubular cell, the oscillations start off with large amplitude at low methane concentrations, and as the methane concentration is increased the cell transitions back into a quasi-steady state. As the transition is occurring, the average current output increases whilst the amplitude of the oscillation decreases. In the model, this corresponds with the stable limit cycle C_S collapsing onto the equilibrium point $\mathbf{e}_-$ as $\bar{a}_0$ increases.

6. Conclusion

In this paper the model presented in [1] was linked with physical parameters in order to compare with the experimental programme set out in Section 4. A diffusion model was implemented based on Lennard-Jones parameters taken from [22] and [23], and expressions for rate constants were presented based on various results from the literature. Additionally, the stoichiometry was detailed in order to link the experimental conditions to the species concentrations in the model.

An experimental programme was carried out using both tubular, and microtubular methane fuelled SOFCs, with a weakly humidified fuel stream. The tubular cells were assembled in-house and the microtubular cell was obtained from the same batch as that in [31]. The test rig and experimental procedure were described in Sections 4.2 and 4.3, and the results were presented in Section 4.4. Finally, the results of the experimental programme were compared with the model in Section 5. It was found that the steady state current output of the cells, as the methane concentration was decreased, matched very well with the steady state hydrogen concentration used in the model, represented by β_-. Both steady and oscillatory states were induced by varying the concentration of methane in the fuel stream in accordance with the model. For lower concentrations of methane, the amplitude of the oscillations was much larger, with the average current output being lower. As the concentration of methane was increased, the oscillations decreased in size whilst the average current output increased, matching well with model predictions. Additionally, it was seen that each of the SOFCs reached a zero current output for a non-zero concentration of methane in the fuel stream. It is important to note that in order to observe the oscillations the step change in methane concentration must be small enough so that the cell does not simply jump from the stable steady state to the zero current output state.

References

[1] J. D. Sands, D. J. Needham, and J. Uddin. A Fundamental Model Exhibiting Nonlinear Oscillatory Dynamics in Solid Oxide Fuel Cells. *Proceedings of the Royal Society A - Mathematical Physical and Engineering Sciences*, 470 (20130551), 2014.

[2] I. D. Kellogg, U. O. Koylu, V. Petrovsky, and F. Dogan. Effectiveness of

Anode in a Solid Oxide Fuel Cell with Hydrogen/Oxygen Mixed Gases. *International Journal of Hydrogen Energy*, 34(12): 5138-5143, 2009.

[3] O. A. Marina, L. R. Pederson, C. A. Coyle, E. C. Thomsen, and D. J. Edwards. Polarization-Induced Interfacial Reactions Between Nickel and Selenium in Ni/Zirconia SOFC Anodes and Comparison with Sulfur Poisoning. *Journal of The Electrochemical Society*, 158(1): B36, 2011.

[4] M. Noponen, M. Halinen, J. Kiviaho, and J. Saarinen. Feasibility of Autothermally Reformed Natural Gas on Anode Supported Solid Oxide Fuel Cells. *Journal of Fuel Cell Science and Technology*, 3(4): 438, 2006.

[5] N. Akhtar, S. P. Decent, D. Loghin, and K. Kendall. Mixed-Reactant, Micro-Tubular Solid Oxide Fuel Cells: An Experimental Study. *Journal of Power Sources*, 193: 39-48, 2009.

[6] M. Mangold, M. Krasnyk, and K. Sundmacher. Nonlinear Analysis of Current Instabilities in High Temperature Fuel Cells. *Chemical Engineering Science*, 59(22-23): 4869-4877, 2004.

[7] Z. Wang, Z. L, B. Wei, K. Chen, X. Huang, W. Pan, and W. Su. Redox of Ni/YSZ Anodes and Oscillatory Behavior in Single-Chamber SOFC Under Methane Oxidation Conditions. *Electrochimica Acta*, 56(19):6688-6695, 2011.

[8] T. Matsui, R. Kishida, J. Y. Kim, H. Muroyama, and K. Eguchi. Performance Deterioration of Ni/YSZ Anode Induced by Electrochemically Generated Steam in Solid Oxide Fuel Cells. *Journal of The Electrochemical Society*, 157(5): B776, 2010.

[9] T. Yoshizumi, S. Taniguchi, Y. Shiratori, and K. Sasaki. Sulfur Poisoning of SOFCs: Voltage Oscillation and Ni Oxidation. *Journal of the Electrochemical Society*, 159(11): F693-F701, 2012.

[10] T. J. Huang, M. C. Huang, W. J. Chen, and C. L. Chou. Oscillation of Electrical Current During Direct Methane Oxidation over Ni-Added LSCF-GDC Anode of Solid Oxide Fuel Cells. *Chemical Engineering Journal*, 153(1-3): 164-169, 2009.

[11] K. Murakami, T. Matsui, R. Kikuchi, H. Muroyama, and K. Eguchi. Activation of LSM Electrode Related to the Potential Oscillation under

Cathodic Polarization. *Journal of The Electrochemical Society*, 157(6): B880, 2010.

[12] S. C. Singhal and K. Kendall. *High Temperature Solid Oxide Fuel Cells: Fundamentals, Design and Applications.* Elsevier Advanced Technology, Oxford, 2003.

[13] A. Dicks. Advances in catalysts for internal reforming in high temperature fuel cells. *Journal of Power Sources*, 71(1-2): 111-122, 1998.

[14] E. S. Hecht, G. K. Gupta, H. Zhu, A. M. Dean, R. J. Kee, L. Maier, and O. Deutschmann. Methane Reforming Kinetics Within a Ni/YSZ SOFC Anode Support. *Applied Catalysis A: General*, 295(1): 4051, 2005.

[15] J. Park, P. Li, and J. Bae. Analysis of Chemical, Electrochemical Reactions and Thermofluid Flow in Methane-Feed Internal Reforming SOFCs: Part I - Modeling and Effect of Gas Concentrations. *International Journal of Hydrogen Energy*, 37: 8512-8531, 2012.

[16] T. X. Ho, P. Kosinski, A. C. Hoffman, and A. Vik. Numerical Analysis of a Planar Anode-Supported SOFC with Composite Electrodes. *International Journal of Hydrogen Energy*, 34: 3488-3499, 2009.

[17] H. Yakabe, M. Hishinuma, M. Uratani, Y. Matsuzaki, and I. Yasuda. Evaluation and Modeling of Performance of Anode-Supported Solid Oxide Fuel Cell. *Journal of Power Sources*, 86(1-2): 423-431, 2000.

[18] P. Gray and S. K. Scott. *Chemical Oscillations and Instabilities: Non-Linear Chemical Kinetics*. International Series of Monographs on Chemistry. Clarendon Press, 1994.

[19] G. M. Goldin, H. Zhu, R. J. Kee, D. Bierschenk, and S. A. Barnett. Multidimensional Flow, Thermal, and Chemical Behavior in Solid-Oxide Fuel Cell Button Cells. *Journal of Power Sources*, 187(1): 123-135, 2009.

[20] S. M. Vora B. I. Bhatt. *Stoichiometry (4th edition)*. Tata McGraw-Hill, 2006.

[21] R. B. Bird, W. E. Stewart, and E. N. Lightfoot. *Transport Phenomena (2nd edition)*. John Wiley & Sons Inc., New York, 2002.

[22] E. A. Mason and L. Monchick. Transport Properties of Polar-Gas Mixtures. *Journal of Chemical Physics*, 36: 2746-2757, 1962.

[23] J. Y. Roncin. Intermolecular Potential Parameters of Some Electronic Excited States of Atoms and Molecules. *Chemical Physics Letters*, 3(6): 408-410, 1969.

[24] K. Hou and R. Hughes. The Kinetics of Methane Steam Reforming over a Ni/α-Al2O Catalyst. *Chemical Engineering Journal*, 82: 311-328, 2001.

[25] J. M. Klein, Y. Bultel, S. Georges, and M. Pons. Modeling of a SOFC Fuelled by Methane: From Direct Internal Reforming to Gradual Internal Reforming. *Chemical Engineering Science*, 62(6): 1636-1649, 2007.

[26] W. Lehnert, J. Meusinger, and F. Thom. Modelling of Gas Transport Phenomena in SOFC Anodes. *Journal of Power Sources*, 87(1-2): 5763, 2000.

[27] E. Achenbach and E. Riensche. Methane/steam Reforming Kinetics for Solid Oxide Fuel Cells. *Journal of Power Sources*, 52: 283-288, 1994.

[28] W. Kong, H. Zhu, Z. Fei, and Z. Lin. A Modified Dusty Gas Model in the Form of a Ficks Model for the Prediction of Multicomponent Mass Transport in a Solid Oxide Fuel Cell Anode. *Journal of Power Sources*, 206: 171-178, 2012.

[29] H. Sumi, R. Kishida, J. Y. Kim, H. Muroyama, T. Matsui, and K. Eguchi. Correlation Between Microstructural and Electrochemical Characteristics during Redox Cycles for Ni/YSZ Anode of SOFCs. *Journal of The Electrochemical Society*, 157(12): B1747, 2010.

[30] R. E. Sonntag, C. Borgnakke, and G. J. Van Wylen. *Fundamentals of Thermodynamics (5th edition)*. John Wiley & Sons, Inc., USA, 1998.

[31] A. Dhir and K. Kendall. Microtubular SOFC Anode Optimisation for Direct Use on Methane. *Journal of Power Sources*, 181(2): 297-303, 2008.

[32] A. Dhir. *Improved Microtubular Solid Oxide Fuel Cells. PhD thesis*, University of Birmingham, 2008.

[33] H. Lu, L. Rihko-Struckmann, and K. Sundmacher. Spontaneous Oscillations of Cell Voltage, Power Density, and Anode exit CO Concentration in a PEM Fuel Cell. *Physical Chemistry Chemical Physics : PCCP*, 13(40): 18179-85, 2011.

[34] M. Bavarian, M. Soroush, I. G. Kevrekidis, and J. B. Benziger. Mathematical Modeling, Steady-State and Dynamic Behaviour, and Control of Fuel Cells: A Review. *Industrial & Engineering Chemistry Research*, 49(17): 7922-7950, 2010.